

A 2-D model for friction of complex anisotropic surfaces

Gianluca Costagliola^a, Federico Bosia^a, Nicola M. Pugno^{b,c,d,*}

^a *Department of Physics and Nanostructured Interfaces and Surfaces Centre, University of Torino,
Via Pietro Giuria 1, 10125, Torino, Italy.*

^b *Laboratory of Bio-Inspired & Graphene Nanomechanics, Department of Civil, Environmental and
Mechanical Engineering, University of Trento, Via Mesiano, 77, 38123 Trento, Italy*

^c *School of Engineering and Materials Science, Queen Mary University of London, Mile End Road,
London E1 4NS, UK*

^d *Ket Labs, Edoardo Amaldi Foundation, Italian Space Agency, Via del Politecnico snc, 00133 Rome,
Italy*

Abstract

The friction force observed at macroscale is the result of interactions at various lower length scales that are difficult to model in a combined manner. For this reason, simplified approaches are required, depending on the specific aspect to be investigated. In particular, the dimensionality of the system is often reduced, especially in models designed to provide a qualitative description of frictional properties of elastic materials, e.g. the spring-block model. In this paper, we implement for the first time a two dimensional extension of the spring-block model, applying it to structured surfaces and investigating by means of numerical simulations the frictional behaviour of a surface in the presence of features like cavities, pillars or complex anisotropic structures. We show how friction can be effectively tuned by appropriate design of such surface features.

Keywords: Friction, Numerical models, Microstructures, Anisotropic materials

1. Introduction

The frictional behavior of macroscopic bodies arises from various types of interactions occurring at different length scales between contact surfaces in relative motion. While it is clear that their ultimate origin lies in inter atomic forces, it is difficult to scale these up to the macroscopic level, including other typical phenomena such as surface roughness, elasticity or plasticity, wear and specific surface structures [1][2]. Moreover, the dependency on “external parameters”, e.g. relative velocity of the surfaces and normal pressure, is neglected in approximate models such as the Amontons-Coulomb law, but violations have been observed [3][4].

For this reasons, simplified models are required for theoretical studies and numerical simulations, and friction problems can be addressed in different ways depending on the

*Corresponding author

Email addresses: gcostagl@unito.it (Gianluca Costagliola), fbosia@unito.it (Federico Bosia), nicola.pugno@unitn.it (Nicola M. Pugno)

specific aspects under consideration. In order to improve theoretical knowledge of friction, or to design practical applications, it is not necessary to simulate all phenomena simultaneously together, and a reductionist approach can be useful to investigate individual issues. Thus, despite the improvement in the computational tools, still in most cases is preferable to develop simplified models to describe specific aspects, aiming to provide qualitative understanding of the fundamental physical mechanisms involved.

One of the most used approaches to deal with friction of elastic bodies consist in the discretization of a material in springs and masses, as done e.g. in the Frenkel-Kontorova model [5], or the Burridge-Knopoff model [6], the latter also known as the spring-block model. For simplicity, these models are often formulated in one dimension along the sliding direction, in various versions depending on the specific application. In recent years, interesting results have been obtained with these models, explaining experimental observations [7]-[11]. The extension to two dimensions is the straightforward improvement to better describe a experimental results and to correctly reproduce phenomena in two dimensions. This has already been done for some systems, like the Frenkel-Kontorova model [12][13] and the spring-block model applied to geology [14]-[19], but much work remains to be done for friction of complex and structured surfaces.

The interest of this study lies not only in the numerical modeling of friction in itself, but also has practical purposes: there are many studies relative to bio-inspired materials [20]-[23] or biological materials [24]-[28] that reproduce non-trivial geometries that can not be reduced to one-dimensional structures.

One of the most widely used models is the one dimensional spring-block model, which was originally introduced to study earthquakes [29]-[31] and has also been used to investigate many aspects of dry friction of elastic materials [32]-[39]. In [40] we have extensively investigated the general behavior of the model and the effects of local patterning (regular and hierarchical) on the macroscopic friction coefficients, and in [41] we have extended the study to composite surfaces, i.e. surfaces with varying material stiffness and roughness; finally in [42] we have introduced the multiscale extension of the model to study the statistical effects of surface roughness across length scales.

In this paper, we propose a 2-D extension of the spring-block model to describe the frictional behavior of an elastic material sliding on a rigid substrate. Our principal aim is to compare the results with those obtained in the one-dimensional case and to extend our study to more complex surface structures, e.g. arrangements of cavities or anisotropic structures like those found in biological materials. The two-dimensional spring-block model allows to consider a more realistic situation and captures a variety of behaviors that can be interesting for practical applications. In particular, we emphasize that the friction coefficients of anisotropic surface structures depends non-trivially on the sliding direction.

The paper is organized as follows: in section 2, we present the model, in section 3.1, we discuss the main differences with the one-dimensional case and we explore the role of the parameters without surface structures, highlighting the phenomenology of the model, in section 3.2, we present the results for standard 1-D and 2-D surface structures like grooves and cavities, in sections 3.3 and 3.4, we consider more complex cases of anisotropic surface patterning; finally, in section 4, conclusions and future developments are discussed.

2. Model

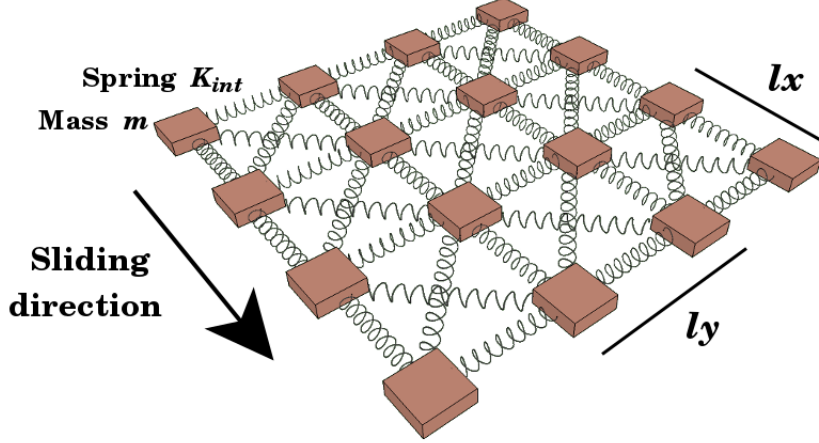


Figure 1: Discretization of a square surface into a 2-D spring-block model, showing the mesh of the internal springs. The shear springs K_s attached above the blocks are not shown.

The equation of motion for an isotropic linear elastic body driven by a slider on an infinitely rigid plane with damping and friction can be written as: $\rho \ddot{u} = \mu \nabla^2 u + (\lambda + \mu) \nabla(\nabla \cdot u) - \gamma \rho \dot{u}$, where u is the displacement vector, ρ is the density, γ is the damping frequency, λ, μ are the Lamé constants. The following boundary conditions must be imposed: the top surface of the body is driven at constant velocity v , the bottom surface is subjected to a spatially variable local friction force, which we discuss below, representing the surface interactions between the elastic body and the rigid plane, while free boundary conditions are set on the remaining sides.

In order to simulate this system, we extend the spring-block model to the two-dimensional case: the contact surface is discretized into elements of mass m , each connected by springs to the eight first neighbors and arranged in a regular square mesh (figure 1) with N_x contact points along the x -axis and N_y contact points along in the y -axis. The distances on the axis between the blocks are, respectively, l_x and l_y . Hence, the total number of blocks is $N_b \equiv N_x N_y$. The mesh adopted in previous studies of the 2-D spring-block model, e.g. [15],[19], does not include diagonal springs, but we add them to take into account the Poisson effect (our mesh is similar to that used in [9]).

In order to obtain the equivalence of this spring-mass system with a homogeneous elastic material of Young's modulus E , the Poisson's ratio must be fixed to $\nu = 1/3$ [43], which corresponds to the plane stress case, $l_x = l_y \equiv l$ and $K_{int} = 3/8 E l_z$, where l_z is the thickness of the 2-D layer and K_{int} is the stiffness of the springs connecting the four nearest neighbor of each block, i.e. those aligned with the axis. The stiffness of the springs connecting a block with the four next-nearest neighbors, i.e. the diagonal springs, must be $K_{int}/2$. Hence, the internal elastic force on the block i exerted by the neighbor j is $\mathbf{F}_{int}^{(ij)} = k_{ij}(r_{ij} - l_{ij})(\mathbf{r}_j - \mathbf{r}_i)/r_{ij}$, where $\mathbf{r}_i, \mathbf{r}_j$ are the position vectors of the

two blocks, r_{ij} is the modulus of their distance, l_{ij} is the modulus of the rest distance and k_{ij} is the stiffness of the spring connecting them.

All the blocks are connected, through springs of stiffness K_s , to the slider that is moving at constant velocity v in the x direction, i.e. the slider vector velocity is $\mathbf{v} = (v, 0)$. Given the initial rest position \mathbf{r}_i^0 of block i , the shear force is $\mathbf{F}_s^{(i)} = K_s(\mathbf{v}t + \mathbf{r}_i^0 - \mathbf{r}_i)$. We define the total driving force on i as $\mathbf{F}_{mot}^{(i)} = \sum_j \mathbf{F}_{int}^{(ij)} + \mathbf{F}_s^{(i)}$. The stiffness K_s can be related to the macroscopic shear modulus $G = 3/8E$, since all the shear springs are attached in parallel, so that by simple calculations we obtain $K_s = K_{int}l^2/l_z^2$. In the following, for simplicity we fix $l_z = l$. This formulation, commonly used in spring-block models, neglects the long-range interactions that may arise from wave propagation through the bulk [44]-[47]. Here, we suppose that the local interactions are dominating, which is a reasonable assumption for slow sliding velocities typical of the experiments we use as benchmarks [20]-[23]. This assumption has already allowed to obtain correct descriptions of the phenomena occurring at the transition from static to dynamic friction [32][38].

The interactions between the blocks and the rigid plane can be introduced in many ways: in the original paper on the spring block model [6] and in earthquake related papers, e.g. [15][18], it is introduced by means of an effective velocity-dependent force [48][49], in friction studies, e.g. [11][32], by springs that attach and detach during motion, in [9][19] by means of the classical Amontons-Coulomb (AC) friction force. These various approaches give rise to slightly different quantitative results, but if they are implemented under reasonable assumptions, they do not significantly affect the overall predictions of the model, which is thought to provide a qualitative understanding of the basic mechanisms of friction. This is true at least for the small sliding velocities we are considering compared to the characteristic velocity scales of the system, i.e. $l\sqrt{K_{int}/m}$. A different qualitative behavior may arise for higher sliding velocities, as shown for rate-and-state friction laws [50]-[52]. In these cases, a careful evaluation of the interplay between the friction law and sliding velocity of the system must be performed.

In this study, we adopt a spring-block model based on the AC friction force and a statistical distribution on the friction coefficients [40]-[42]: while the block i is at rest, the friction force $\mathbf{F}_{fr}^{(i)}$ opposes to the total driving force, i.e. $\mathbf{F}_{fr}^{(i)} = -\mathbf{F}_{mot}^{(i)}$, up to a threshold value $F_{fr}^{(i)} = \mu_{s_i} F_n^{(i)}$, where μ_{s_i} is the static friction coefficient and $F_n^{(i)}$ is the normal force on i . When this limit is exceeded, a constant dynamic friction force opposes the motion, i.e. $\mathbf{F}_{fr}^{(i)} = -\mu_{d_i} F_n^{(i)} \hat{\mathbf{r}}_i$, where μ_{d_i} is the static friction coefficient and $\hat{\mathbf{r}}_i$ is the velocity direction of the block. In the following we will drop the subscript s, d every time the considerations apply to both the coefficients.

The friction coefficients are extracted from a Gaussian statistical distribution to account for the randomness of the surface asperities, i.e. $p(\mu_i) = (\sqrt{2\pi}\sigma)^{-1} \exp[-(\mu_i - (\mu)_m)^2/(2\sigma^2)]$, where $(\mu)_m$ denotes the mean of the microscopic friction coefficients and σ is its standard deviation. In order to simulate the presence of patterning or of structures on the surface, we set to zero the friction coefficients of the blocks located on zones detached from the rigid plane. The microscopic static and dynamic friction coefficients are fixed conventionally to $(\mu_s)_m = 1.0(1)$ and $(\mu_d)_m = 0.50(5)$, respectively, where the numbers in brackets denote the standard deviations of their Gaussian distributions.

The macroscopic friction coefficients are denoted with $(\mu)_M$. The static friction coefficients is calculated from the first maximum of the total friction force, while the dynamic

one as the time average over the kinetic phase. To calculate the friction coefficients as ratio between longitudinal force and normal force, the norm of the longitudinal force vector must be calculated. When calculating time averages, care must be taken in the order of the operations, if there is an inversion of the friction force (i.e. some blocks exceed the rest position, as in the analytical calculations of [40]) or a periodic motion takes place, switching the operations of norm and time average produces different results. In these cases, the calculation closer to the realistic experimental procedure must be adopted. However, in the following results, we have checked that the above conditions do not occur and the order of the operations is irrelevant. The model does not include roughness variations during sliding or other long term effects, so that the results for dynamic friction are to be considered within the limits of this approximation

A damping force is added to eliminate artificial block oscillations: in [32] and in the papers based on it (e.g. in [39]) this is done by means of a viscous damping force proportional to the velocity of the block, i.e. $\mathbf{F}_d^{(i)} = -\gamma m \dot{\mathbf{r}}_i$. However, there is another option, e.g. in the 2-D model in [9], where the damping is imposed on the block oscillations between each pair of blocks i and j , i.e. $\mathbf{F}_d^{(ij)} = -m\gamma (\dot{\mathbf{r}}_i - \dot{\mathbf{r}}_j)$, thus emulating the description usually adopted for viscoelastic materials [53]-[58]. In section 3.1, we discuss the different behavior obtained with the two approaches, but in the following of the study we adopt the former one, which is the simplest to allow damping of non physical oscillations.

Thus, the complete equation of motion for the block i is: $m\ddot{\mathbf{r}}_i = \sum_j \mathbf{F}_{int}^{(ij)} + \mathbf{F}_s^{(i)} + \mathbf{F}_{fr}^{(i)} + \mathbf{F}_d^{(i)}$. The overall system of differential equations is solved using a fourth-order Runge-Kutta algorithm. In order to calculate the average of any observable, the simulation must be iterated, extracting each time new random friction coefficients. In repeated tests, an integration time step $h = 10^{-8} s$ proves to be sufficient to reduce integration errors under the statistical uncertainty in the range adopted for the parameters of the system.

We consider only a square mesh, i.e. $N_x = N_y \equiv N$, and we will specify the number of blocks for each considered case. The default normal pressure is $P = 0.05$ MPa, so that the normal force on each block is $F_n^{(i)} = Pl^2$ and the total normal force is $F_n = Pl^2 N^2$. The slider velocity is $v = 0.05$ cm/s. We will discuss in section 3.1 the motivations for these choices, but in any case the results display small dependence on these parameters.

Realistic macroscopic elastic properties are chosen, e.g. a Young's modulus $E = 10$ MPa, which is typical for a soft polymer or rubber-like material and a density $\rho = 1.2$ g/cm³. The distance between blocks l in the model is an arbitrary parameter representing the smallest surface feature that can be taken into account and it is chosen by default as $l = 10^{-3}$ cm, so that the order of magnitude matches those typical of surface structures used in experiments [20]-[23].

3. Results

3.1. Non-patterned surface

In this section, we model friction problems relative to homogeneous, non-patterned surfaces varying the fundamental parameters to understand the overall behavior and to compare it with that of the 1-D model studied in [40]. In figure 2, the friction force behavior as a function of time is shown with the default set of parameters: there is the linearly growing static phase, up to the macroscopic rupture event, followed by the dynamic phase in which the system slides with small stick-slip oscillations at constant velocity v . The percentage of blocks in motion as a function of time is also shown: in the kinetic phase, single blocks or small groups slip simultaneously but not in a synchronized manner with respect the rest of the surface.

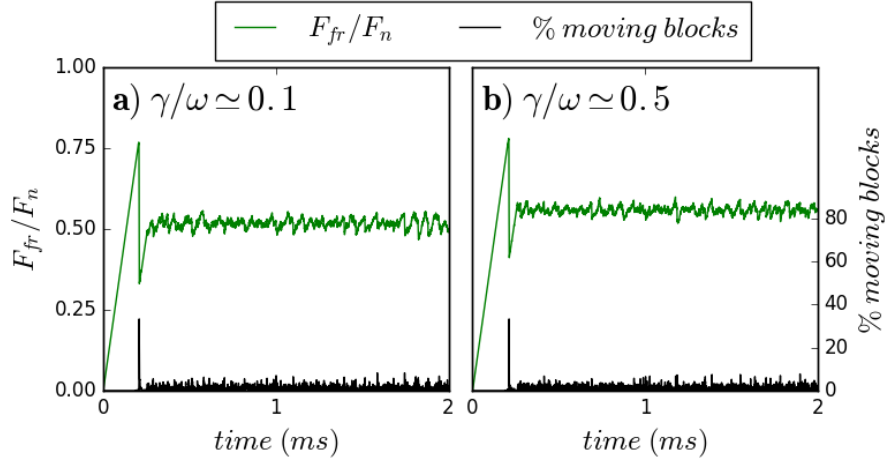


Figure 2: Time evolution for the total friction force and percentage of moving blocks for $N = 20$, pressure $P = 0.1$ MPa, velocity $v = 0.1$ cm/s, $\gamma/\omega = 0.1$ (a) or $\gamma/\omega = 0.5$ (b), where ω is the internal frequency $\omega \equiv \sqrt{K_{int}/m}$. The other parameters are set to the default values. Greater damping enhances the dynamic friction coefficient and reduces stick-slip oscillations.

The first difference with the 1-D model is that the 2D array of springs shown in figure 1 allows to simulate the Poisson effect, i.e. a deformation in the transversal direction due to the stretching in the longitudinal one. Secondly, due to the model definition explained in section 2, the stiffnesses do not depend on the total number of blocks, so that increasing N does not modify the elastic properties, but only the size of the system. Since the number of points grows as the square of the side, $N \gtrsim 100$ can already be considered a large system, as shown in figure 3, where the size effects on the global static friction coefficient are shown. Similar results hold for the dynamic friction. In the left panel (figure 3a) and in the right panel (figure 3b), the influence of the applied pressure P and the slider velocity v is also shown, respectively. In the typical ranges of these parameters, variations are limited within few percent, so that in the following we adopt typical values, e.g. $v = 0.05$ cm/s and $P = 50$ KPa without further discussions about their influence.

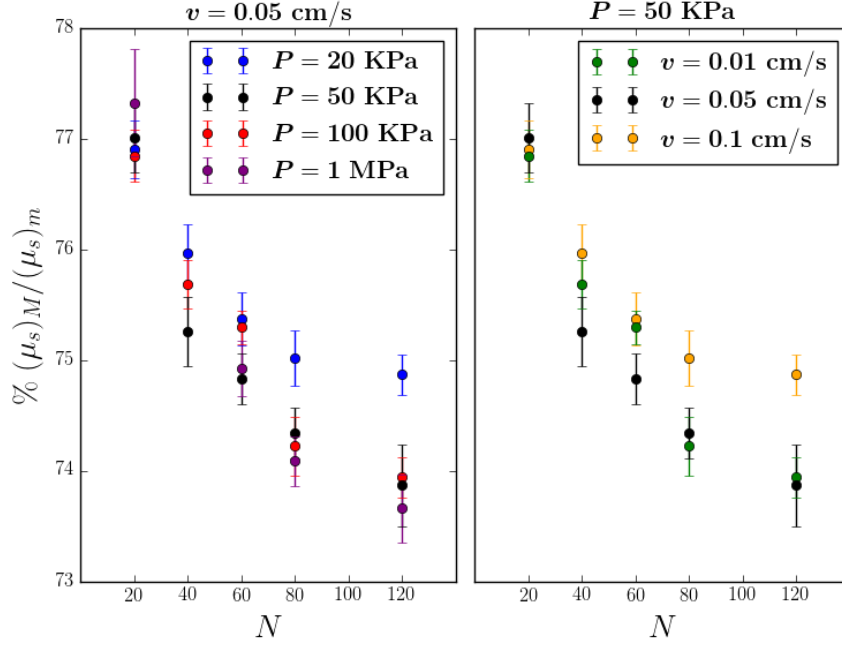


Figure 3: Static friction coefficient as a function of the number of blocks N by varying the applied pressure P with the default velocity $v = 0.05 \text{ cm/s}$ (a), and by varying the velocity v with the default pressure $P = 50 \text{ KPa}$ (b). Thus, the black dots on both sides show the curve for the default set of parameters. Variations with respect to this are limited to few percent in the typical ranges of these parameters.

3.1.1. Role of damping

As mentioned, two possible approaches can be adopted to introduce viscous damping in the model. If we introduce a viscous damping force on the velocity, i.e. $\mathbf{F}_d^{(i)} = -\gamma m \mathbf{\dot{r}}_i$, there is an increase on the dynamic friction coefficient due to the damping which reduces the slip phases, similarly to the effect observed in [40]. This does not affect the general behavior of the system, as long as γ is in underdamped regime, i.e. $\gamma < \omega \equiv \sqrt{K_{int}/m}$.

The other option consists in assuming the damping to be dependent on the relative oscillations between blocks, i.e. $\mathbf{F}_d^{(ij)} = -m\gamma (\mathbf{\dot{r}}_i - \mathbf{\dot{r}}_j)$, thus reproducing the generalized Maxwell model for viscoelastic materials. This radically changes the previously-described kinetic phase: for small damping values, there is a limited increase of the dynamic friction with small stick slip events, but for large damping, the fluctuations become larger and the kinetic phase consists in collective slips of the whole surface (figure 4). The explanation for this is that this type of damping favours the elimination of relative block oscillations, enhancing the coherence of the system, so that sliding events can involve a large number of blocks also during the kinetic phase.

This behavior is highly non-trivial, since it is influenced not only by the sliding velocity or the elastic properties of the surface, but also by the discretization parameters, i.e. the

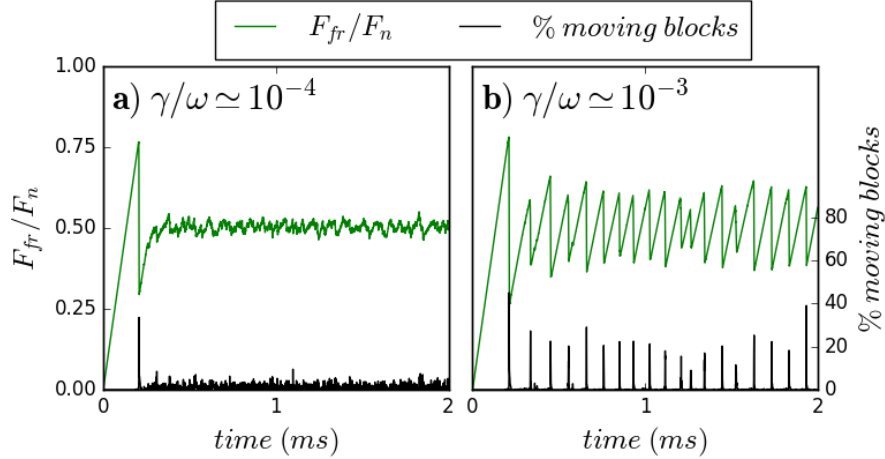


Figure 4: Time evolution for the total friction force with the same parameters of figure 2, except that the damping is imposed on the relative velocity between neighboring blocks, i.e. using a viscoelastic material model, respectively with $\gamma/\omega = 10^{-3}$ (a) or $\gamma/\omega = 10^{-4}$ (b), where ω is the internal frequency ($\omega \equiv \sqrt{K_{int}/m}$). The static friction coefficient remains unchanged, but the kinetic phase is totally different, in particular for higher damping values there are greater stick-slip oscillations.

number of blocks N : for example, with $N = 80$, the stick-slip oscillations are reduced, since for larger systems it is difficult to obtain collective slips and it is more likely that different portions of the surfaces move independently.

Thus, the model can describe a variety of different situations and can capture the richness of behaviour of the viscoelastic material. In the following, we adopt the first solution, i.e. a viscous damping force on the velocity of the blocks, since it provides a simpler approach for damping artificial block oscillations, and we fix $\gamma = 500 \text{ ms}^{-1}$ ($\gamma/\omega \simeq 0.1$).

3.1.2. Detachment fronts

In this section, we focus on the transition from static to dynamic friction, corresponding to the maximum of the total friction force and the following drop in figure 2. The spring-block model has been used in many recent studies to obtain valuable insights on this aspect [8]-[11] and confirming fundamental experimental observations about the onset of the dynamic motion [7],[59]-[61]. Our aim is not a detailed study of the wave propagation and the rupture fronts before the sliding, for many accurate works have been produced on these topics [62]-[67], but to show how the 2-D model allows to qualitatively predict the phenomena illustrated in the literature.

In figure 5, four snapshots of the longitudinal deformation on the surface at different times of the transition are shown: starting from the points with the weakest static friction thresholds, rupture fronts propagate on the surface, until the whole surface slides (see the caption of figure 5 for a detailed description). The maximum force, i.e. the point in which the global static friction coefficient is calculated, takes place when the first rupture front begins its propagation; then the blocks are progressively reached by the fronts and relax, corresponding to the phase with the drop of the friction force. This decrease ends

when the whole surface has been reached by the rupture fronts and the overall sliding motion begins. At the beginning of the sliding, the spring mesh is frozen in a non-uniform distribution of regions of compression and tension. These regions tend to relax during the subsequent kinetic phase, in which different portions of the surface have continuous but incoherent stick-slip motion, and regions of residual stress remain. This has already been noted in the 1-D model [32] and observed experimentally [7], in terms of "memory effects" after the transition to kinetic friction [37]. The surface deformation during the transition from static to dynamic friction is illustrated in Video 1 together with the time evolution of the friction force.

In 2-D models, the shape of the rupture front in the horizontal plane can be studied: before the nucleation of a front, the detachment propagates first to the neighbors of the weakest threshold point along the sliding direction, so that the nucleation region is not a single point, but more likely a segment. For this reason, the fronts in figure 5 display an elliptical shape.

Many details of these simulations depend on the chosen parameters: the thresholds distribution, which is a way to parametrize the surface roughness, but also the velocity and the elasticity of the material affect the number of fronts, the speed of propagation and the duration of the friction force decrease. Moreover, the model does not take into account the modification of the effective contact area during the transition. However, it is evident that the avalanche of ruptures originate from the regions with weakest thresholds and then propagates to the whole surface in all the directions, similarly to avalanches in fracture mechanics [8],[63]. Also, it is interesting to note the non-trivial persistence of residual deformations in correspondence with the regions of interaction between multiple waves, deriving from the inelastic nature of the model.

The role of the weakest thresholds is confirmed also in [41], where it is shown that the distribution of the static friction thresholds deeply affect the global static friction and the onset of motion, while it is almost irrelevant for the dynamic phase. Thus, in a real material the nucleation points could be the contact points with imperfect contact on the surface. On the basis of this observation, we discuss in the next sections how static friction can be radically modified by structures that give rise to non-trivial stress distributions on the surface before the sliding phase.

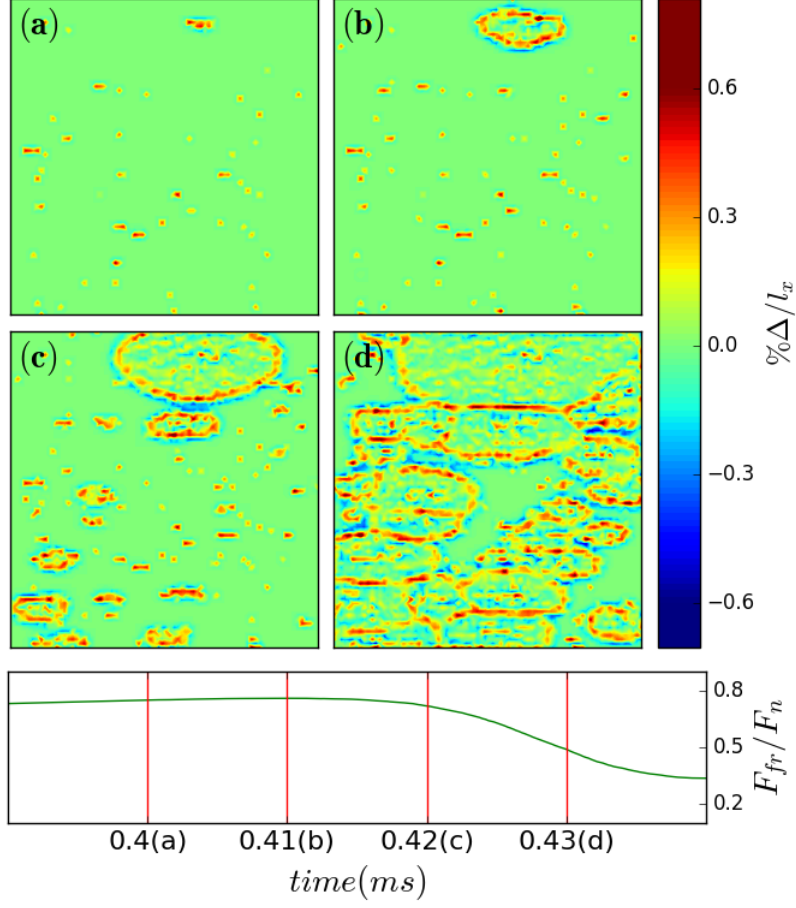


Figure 5: Time snapshots of the spring mesh deformation Δ along the longitudinal direction on the surface divided by the block distance l_x , so that positive values (red) indicate compression and negative values (blue) tension. Before the maximum of the friction force is reached, some blocks with weak static friction thresholds detach (a), then a rupture front nucleates from the weakest point, corresponding to the instant of the maximum force before the drop (b); the front propagates while other fronts nucleate elsewhere (c) finally, the whole surface slides leaving a non-uniform distribution of regions under tension/compression (d).

3.2. Patterned structures

First we consider single-level surface structures, i.e. described by only one characteristic length scale, such as those shown in figure 6. The 2-D surface allows to simulate more configurations than those studied in the one dimensional case, e.g. in [40], which is limited to structures similar to figure 6a. In experimental tests [20], grooves aligned with the sliding direction, like those in figure 6b, have also been considered, while square cavities and square pillars (figure 6c and 6d, respectively), are the simplest two dimensional structures that we can consider. Similar structures have been investigated experimentally [68]-[70].

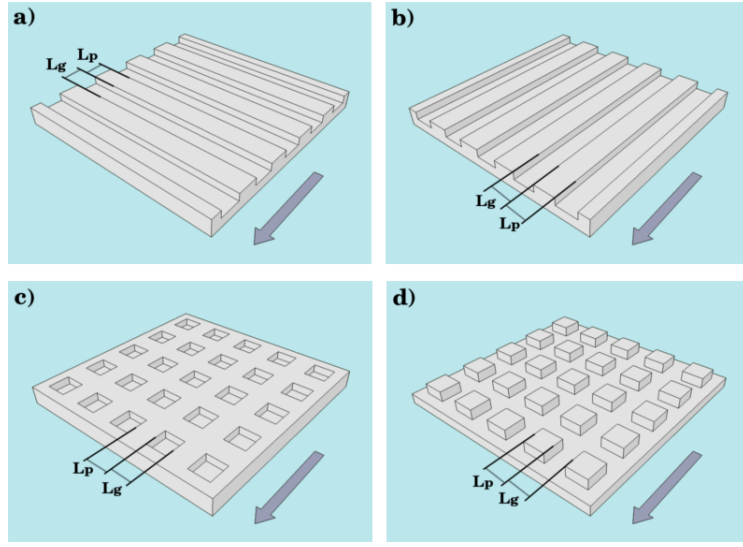


Figure 6: Single-level surface structures considered in the simulations: patterning with grooves in direction perpendicular (a) or parallel (b) to the motion. Square cavities (c) and pillars (d). The number $n_g \equiv L_g/l_x$ is the ratio between the size of the structure and the elementary block distance. The arrow denotes the sliding direction. The patterns are modelled as 2-D surfaces but graphically represented as 3-D structures for illustrative purposes.

In order to simulate these structures, we set to zero the friction coefficients of the blocks corresponding to regions no longer in contact with the sliding plane. This is a 2-D model of the structures shown in 6, in which grooves correspond to regions without friction, while effects occurring in the depth direction are neglected, e.g. mechanical interlocking, geometric nonlinearities, and variability in stresses normal to the surface. However, this does not modify our general conclusions. To characterize the stress state of the surface, we define the surface stress field $\sigma \equiv F_{mot}/l^2$, which in the static phase is equivalent to the tangential stress F_{fr}/l^2 for the regions in contact with the substrate. In the following, unless otherwise stated, we indicate as "stress" the modulus of σ , while we denote with σ_x and σ_y its components along the x- and y-axis, respectively.

We denote with L_g the width of generic non contact regions, like grooves or holes, and with L_p the width of contact regions, like pillars or pawls, as shown in figure 6. The ratios $n_g \equiv L_g/l_x$ and $n_p \equiv L_p/l_x$ represent the number of blocks contained in

these regions, which are convenient adimensional numbers to classify the width of the structure. In the following, if only n_g is reported, we are considering the case $n_g = n_p$. The system parameters are fixed to the default values with $N_x = N_y = 120$.

3.2.1. Static Friction

In [40] we have shown that in the static phase, i.e. before every block begins to slide, the in-plane surface stress is mostly concentrated at the edge of the grooves. Here, the same results are obtained and, more in general, we observe that stresses are concentrated at the edges of the structure in both directions, as shown in figure 7 for the configuration of cavities. Due to the Poisson effect, stress components also appear in the transversal direction. For example, the structures in figure 6c tends to be deform as a trapezoid with the greater basis in the forward direction. Similar deformations occur in the case of grooves or other rectangular shapes. Vice versa, a square pillar structure such as in figure 6d deforms like a trapezoid with the smaller basis in the forward direction. Video 2 illustrates the time evolution of the total friction force and the longitudinal component of the surface stress distribution in the case of square cavities with $n_g = 10$ (as in figure 7).

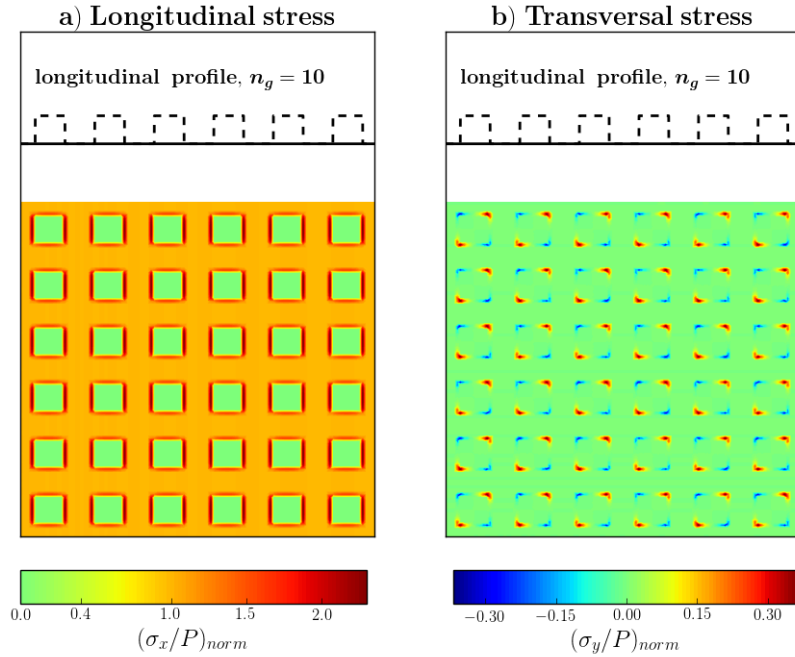


Figure 7: Longitudinal (a) and transversal stress (b), divided by the pressure on the 2-D surface, before the blocks motion, for a structure with square cavities as in figure 6c and $n_g = 10$ (the dotted lines above shows the surface profile). The stress-pressure ratio is also normalized with the value obtained for a smooth surface, so that, for example, the normalized value is fixed to one for non-edging blocks. The stress is accumulated at the edge of the cavities with a non-zero component in the transversal direction.

For a generic structure, the total stress is mostly concentrated where concave angles

are present and where non-negligible stress components are present in both directions. From this we deduce that, other parameters being equal, a structure with a great number of concave angles and a large perimeter is expected to have considerably reduced static friction. Practical examples of such structures are presented in the next section 3.3.

Results are shown in figure 8: in the case of patterning there is the well known decrease in static friction for larger grooves, however in this case the behaviour is not monotonic. The explanation for this is that, during the rupture process, the stress is redistributed on the surface in a non trivial way: in the 1-D system, once the force thresholds of the edge blocks are exceeded, the stress is transferred only to the blocks adjacent to the edge, thus increasing the groove width but keeping the patterned structure. In 2-D, instead, ruptures can be distributed in different parts along the transversal direction, so that the edge formed by the attached blocks is no longer a regular patterning, but could be, for example, a winding profile with a non-trivial stress distribution. This influences the transition from static to dynamic friction and, accordingly, the maximum of the total friction force. Videos 3 and 4 illustrate the time evolution of the total friction force and surface stress distribution (longitudinal component) in the case of transversal and longitudinal grooves, respectively, with $n_g = 2$.

In other terms, the crack front is forced to propagate along the pawls. When they are narrow, i.e. for small n_g , their dynamics is practically one-dimensional. If they are wider, the dynamics is determined by interactions of rupture fronts in different directions, so that the overall behavior is more complicated and a non-monotonic dependence of static friction n_g can arise. Moreover, before the sliding phase, the stress on the edges aligned with the sliding direction is slightly smaller than that on transversal ones, but the global static friction is larger for transversal grooves with respect to longitudinal ones (figure 8). This can be only ascribed to the transition from static to dynamic friction: as noted in section 3.1.2, the detachment front propagates first to the neighbors along the sliding direction, so that in the case of transversal grooves, the wave propagation is hampered due to the small pawl size, despite the stress being slightly larger. This is less influential for large n_g values and, indeed, the static friction is greater for longitudinal grooves. Overall, the interpretation of particular behaviors related to specific structures requires a detailed analysis of the onset of the dynamic motion for each specific case.

The static friction coefficient for square cavities is the smallest of the considered structures one for $n_g \leq 4$, but it does not decrease as significantly as for other structures again for larger cavities; a similar behaviour has been observed experimentally for bulk metal glass materials with honeycomb holes [23], suggesting that the origin of the behaviour is related to the stress distribution determined by its structure rather than by the material.

Finally, the square pillars with regular spacing have highest static friction for small n_g , but the smallest one for large n_g . The effective contact area for this structure is $S/S_{tot} = 1/4$, so that the static friction thresholds are doubled with respect the regular patterning. However, for larger pillars, the stress on the edges and concave angles (contrary to hole structures) increases and consistently with the argument above, the friction coefficient is reduced.

The static friction of such structures is qualitatively controlled by the width of the spacings (in our case n_g) and the effective contact area as in the 1-D case, but also by its shape and the orientation with respect to the sliding direction. In order to understand quantitatively which geometrical feature prevails, an accurate study of the stress distribution before the sliding and of the transition from static to dynamic friction is required,

since in general simple proportionality laws cannot be formulated.

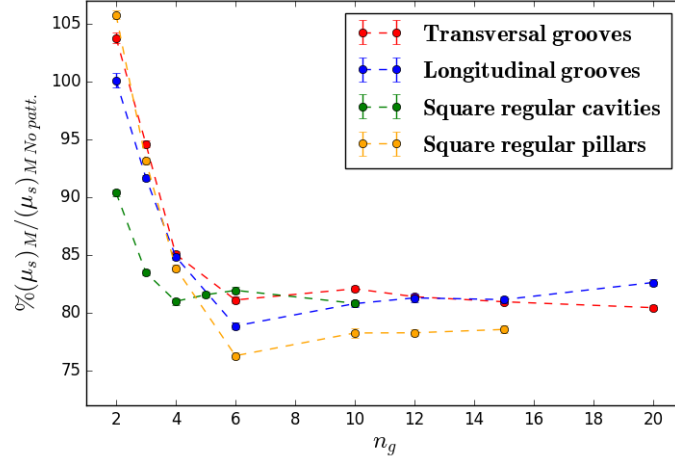


Figure 8: Normalized static friction coefficients for the four single-level structures of figure 6. Results are normalized with respect to the static friction coefficients for a smooth surface (non-patterned case) and are displayed as a function of the structure characteristic width $n_g = n_p$. Notice the decrease of static friction for $n_g \simeq 2$ and the non monotonic behavior for larger sizes ($n_g > 6$).

3.2.2. Dynamic friction

The dynamic friction coefficient in the presence of the considered structures displays small relative variations with respect to the non-patterned case. However, a trend can be observed, as reported in figure 9: the dynamic friction coefficients are always increased with respect the non-patterned case, and are reduced by increasing the size of the structures. This can be explained by considering that in this regime the dynamic motion entails the non-synchronized sliding of different parts of the surface, with an equilibrium between moving and stationary blocks. If the level of stress increases, there are more blocks moving and fewer subjected to static friction, so that the sum of the friction forces during sliding, which determines the total dynamic friction coefficient, decreases with n_g .

Comparing the four different structure types, the dynamic friction coefficients increases by reducing the effective contact area, as noted in [40], but the geometry is also influential: the different behavior for longitudinal and transversal grooves, as explained for static friction, influences also the dynamic friction due to the blocks at rest during the dynamic phase.

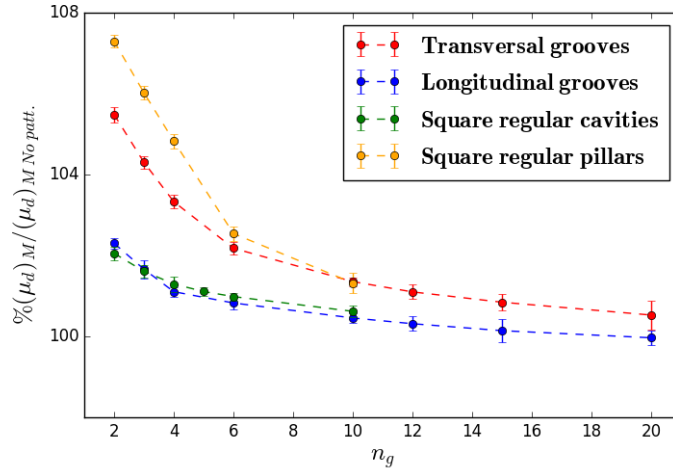


Figure 9: Normalized dynamic friction coefficients for the four single-level structures of figure 6. Results are normalized with respect to the dynamic friction coefficients for a smooth surface (non-patterned case) and are displayed as a function of the structure typical width $n_g = n_p$. The decreasing trend with the size of the structures is limited to few percent with respect the non-patterned case.

3.3. Winding tread patterns

As observed in the previous section, with a general non-trivial surface structure, the stress concentrations before the sliding is distributed at the edges and at the concave angles, so that for winding tread patterns we expect reduced static friction. This is confirmed by simulation on structures such as those shown in figure 10, in which the real contact area is the same of equal spaced grooves in figure 6a,b, but concave angles and perimeter are increased due to the winding profile of the grooves.

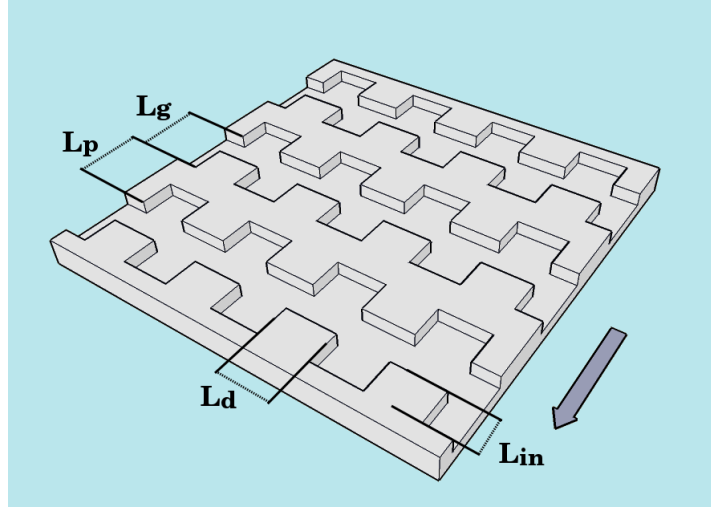


Figure 10: Structure derived from that in figure 6a, in which the straight edge of the grooves has been modified to a winding profile with ratchets of width L_d and depth L_{in} . The effective contact area is halved, like in the case of regular patterning with grooves and pawls of the same size.

As observed in [40], the effective contact area and the width of the spacings affect static friction too. Thus, in order to design a surface with a desired static friction coefficient, all of these three factors need to be considered. We consider for simplicity the case of figure 10 varying the size of the features: as in the previous section, L_g is the spacing between two consecutive structures along the sliding direction and L_p is the width of the structure. L_d is the width of the ratchets in the transversal direction to the sliding one and L_{in} is their indentation. By dividing these values by l_x , the values n_d and n_{in} are obtained, corresponding to the number of blocks for each feature in the width and length direction, respectively.

In figures 11 and 12 the friction coefficients of the various tread patterns are shown and, in the table 1, their legend is reported. As expected from the previous discussion, static friction can be further reduced with respect to the case of periodic regular patterning with an increase of the perimeter and of the concave angles of the structures. Moreover, the precise value can be manipulated by varying the ratio between depth and width of structure, exploiting the high degree of tunability. There is an optimal configuration to obtain the maximum friction reduction, which involves ratchets whose depth is different than the width (e.g. configurations *s6_10_4* and *s20_4_10* of table 1). The dynamic friction can also be manipulated, although the relative variations are smaller.

Contrarily to the static friction case, these structures can enhance dynamic friction with respect to the corresponding periodic regular structure.

Finally, by rotating the sliding direction perpendicularly to that shown in figure 10, similar qualitative considerations hold, though numerical results vary. For the configurations we have tested, only the *s20_4_10* has the weakest static friction for both the direction. Thus, we can conclude that, by rotating these structures, results are not symmetric, but a configuration with weak the static friction coefficients in both direction can be found.

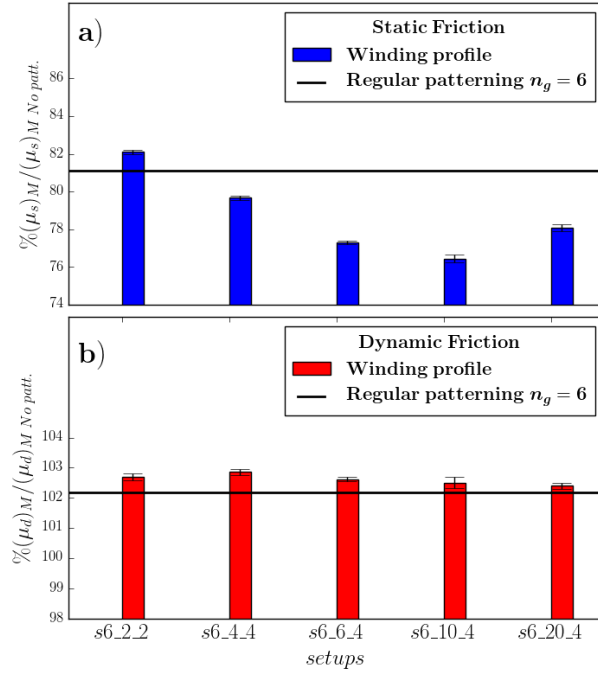


Figure 11: Normalized static (a) and dynamic (b) friction coefficients for the different tread patterns in table 1 compared to those for a regular patterning with $n_g = n_p = 6$ (black line). The static coefficient can be further reduced with respect to the case of periodic regular patterning.

3.4. Anisotropic patterns

In section 3.2, we discussed the different behavior obtained for longitudinal and transversal grooves, i.e. by rotating the grooves with respect to the sliding direction. In this section, we further investigate the role of anisotropic surface structures by considering, for example, rectangular pillars, as shown in figure 13.

By exploiting the mechanisms observed in section 3.2, we find that with this structure static friction can vary significantly by rotating the sliding direction. Results are reported in figure 14, while in table 2 the size of the sides are summarized. The pillar sides are denoted with L_{p_x} , L_{p_y} and their distances with L_{g_x} , L_{g_y} along the x and y axis,

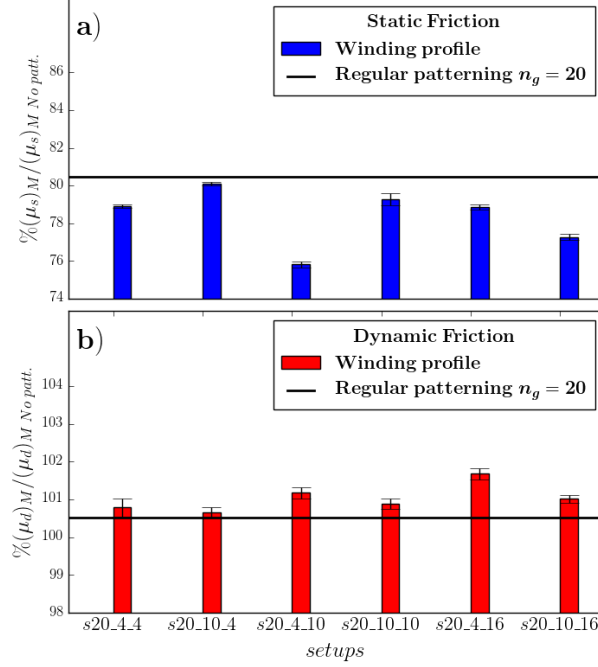


Figure 12: Normalized static (a) and dynamic (b) friction coefficients for the different tread patterns in table 1 compared to those for a regular patterning with $n_g = n_p = 20$ (black line). While the dynamic friction coefficient displays little variation, the static friction coefficient can be remarkably reduced with an optimal combinations of parameters.

tread pattern	grooves n_g	width n_d	depth n_{in}	tread pattern	grooves n_g	width n_d	depth n_{in}
$s6_2_2$	6	2	2	$s20_4_4$	20	4	4
$s6_4_4$	6	4	4	$s20_10_4$	20	10	4
$s6_6_4$	6	6	4	$s20_4_10$	20	4	10
$s6_10_4$	6	10	4	$s20_10_10$	20	10	10
$s6_20_4$	6	20	4	$s20_4_16$	20	4	16
				$s20_10_16$	20	10	16

Table 1: Table reporting the setups of the structure of figure 10 corresponding to the results presented in figures 11 and 12. For all the setups only n_g is reported since $n_p = n_g$.

respectively. Dividing these by the length l , we obtain the ratios n_{p_x} , n_{p_y} , n_{g_x} , n_{g_y} , respectively. For rectangular pillars aligned with the sliding direction there is a remarkable reduction of static friction. Despite this result being intuitive, it is interesting to note the large difference in static friction that is exclusively due to the rotation of the sliding direction. The anisotropy of the structure and the underlying mechanisms occurring at the onset of the sliding determine this behaviour. Thus, it appears that, to manipulate static friction with the sliding direction, anisotropic dimensions of the structure are more

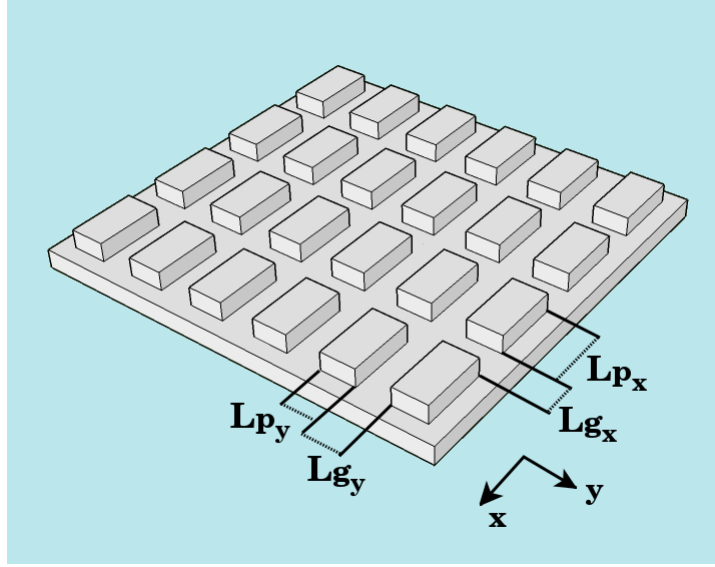


Figure 13: Surface with rectangular pillars of size L_{p_x} , L_{p_y} and placed at L_{g_x} , L_{g_y} along the x and y direction, respectively. This simple configuration displays interesting properties due to the anisotropy by switching the sliding direction between the x and y axis.

effective than complex shapes.

Additionally, we observe that, by increasing the size of the pillars, static friction decreases (as expected), and that the differences between the two directions are also reduced. This confirms that the effect is due to the mechanisms occurring during the transition from static to dynamic friction, as explained for grooves 3.2.

data set	n_{p_x}	n_{p_y}	n_{g_x}	n_{g_y}
s_1	8	2	4	4
s_2	12	3	6	6
s_3	16	4	8	8
s_4	8	2	4	6

Table 2: Characteristics of the anisotropic pillars of figure 13 corresponding to the results presented in figure 14. We denote with n_{p_x} , n_{p_y} the sides the pillars, and with n_{g_x} , n_{g_y} their distances along the x and y axis, respectively, expressed in number of elementary blocks.

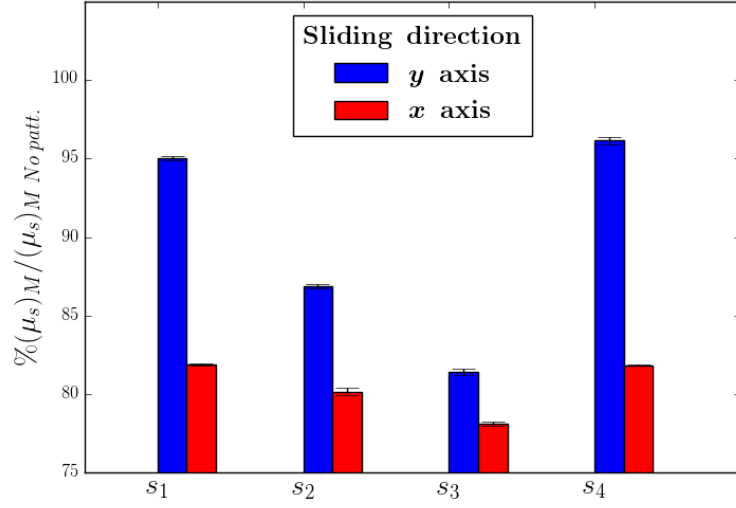


Figure 14: Static friction coefficients for different sizes of anisotropic pillars in 2, normalized by the value for a smooth surface. The x and y axis are defined as in figure 13, i.e. the larger sides of the rectangular pillars are aligned with the x axis. There is a remarkable difference between the static friction coefficients in perpendicular sliding directions.

4. Conclusions

In this paper, we have introduced a 2-D version of the spring-block model to investigate the friction coefficients of complex surfaces that cannot be reduced to one dimension. This model is fundamental for practical applications and to explain recent research results on friction of patterned surfaces in biological and bio-inspired materials. We have described the model in detail and presented benchmark results with a non-patterned surface, illustrating the effects of the model parameters, the general behavior of the system and to its consistency with results from the literature. We have also shown that interesting insights on friction can be obtained by investigating the transition from static to dynamic friction and the propagation of avalanche ruptures on the surface.

Next, we have considered simple patterned surfaces, e.g. longitudinal and transversal grooves, regular square cavities and pillars. Due to the Poisson effect, the in-plane surface stresses are non-zero in the transversal direction, so that structures like cavities deform and stretch in the forward sliding direction, while they undergo compression in the backward one, and vice versa for protruding structures like pillars. The surface stress is mostly concentrated at the edges and at concave angles. We have investigated how the friction coefficient is modified by varying the size of these structures, finding non-trivial behaviors that depend on the surface redistribution of stress during the transition from static to dynamic friction. The most interesting predictions are relative to the non-monotonic behavior of static friction by varying the size of the cavities (in agreement with experimental results) and the maximum static friction reduction obtained for structures with large regular square pillars.

Finally, we have considered winding tread patterns, which have the same contact area and the same spacings of regular groove patterns, but a greater number of concave angles and perimeter. As expected from the previous observations, we find a remarkable static friction reduction for some of these configurations. Thus, to manipulate the global static friction with structured surfaces, while in the 1-D case both the contact area and the width of the structures play a role, in the 2-D case the geometry of the edges also becomes fundamental. Fine tuning of static friction can also be achieved by varying the size of the specimens. Moreover, in the case of anisotropic structures like rectangular pillars, the friction coefficients can vary significantly with the sliding direction, which becomes an additional parameter to take into account. These kinds of predictions require a 2-D model such as the one presented herein that is able of capturing the non-trivial behavior of complex structures similar to those commonly observed in nature or employed in technological fields such as tire tread design.

Acknowledgments

N.M.P. is supported by the European Commission H2020 under the Graphene Flagship Core 1 No. 696656 (WP14 “Polymer Nanocomposites”) and FET Proactive “Neurofibres” grant No. 732344. G.C. and F.B. are supported by H2020 FET Proactive “Neurofibres” grant No. 732344. Computational resources were provided by the Centro di Competenza sul Calcolo Scientifico (C3S) of the University of Torino (c3s.unito.it) and by hpc@polito (<http://www.hpc.polito.it>).

References

References

- [1] B.N.J. Persson, *Sliding Friction - Physical principles and application*, in Nanoscience and Technology, Springer-Verlag Berlin Heidelberg (2000)
- [2] M. Nosonovsky, B. Bhushan, *Multiscale friction mechanisms and hierarchical surfaces in nano- and bio-tribology*, Mater. Sci. Eng. R 58 (2007) 162
- [3] Y. Katano, K. Nakano, M. Otsuki, H. Matsukawa, *Novel Friction Law for the Static Friction Force based on Local Precursor Slipping*, Sci. Rep. 4 (2014) 6324
- [4] Z. Deng, A. Smolyanitsky, Q. Li, X.Q. Feng, R.J. Cannara, *Adhesion-dependent negative friction coefficient on chemically modified graphite at the nanoscale*, Nature Materials 11 (2012) 1032
- [5] O.M. Braun, Y. S. Kivshar, *The Frenkel-Kontorova Model: Concepts, Methods, and Applications*, Springer-Verlag, Berlin (2004)
- [6] R. Burridge and L. Knopoff, *Model and theoretical seismicity*, Bull. Seismol. Soc. Am. 57 (1967) 341
- [7] S.M. Rubinstein, G. Cohen, J. Fineberg, *Detachment fronts and the onset of dynamic friction*, Nature 430 (2004) 1005
- [8] E. Bouchbinder, E.A. Brener, I. Barel, M. Urbakh, *Slow Cracklike Dynamics at the Onset of Frictional Sliding*, Phys. Rev. Lett. 107 (2011) 235501
- [9] J. Trømborg, J. Scheibert, D.S. Amundsen, K. Thøgersen, A. Mälthe-Sørenssen, *Transition from Static to Kinetic Friction: Insights from a 2D Model*, Phys. Rev. Lett. 107 (2011) 074301
- [10] S. Maegawa, A. Suzuki, K. Nakano, *Precursors of Global Slip in a Longitudinal Line Contact Under Non-Uniform Normal Loading*, Tribol. Lett. 38 (2010) 3
- [11] D. S. Amundsen, J. Scheibert, K. Thøgersen, J. Trømborg, A. Mälthe-Sørenssen, *1D Model of Precursors to Frictional Stick-Slip Motion Allowing for Robust Comparison with Experiments*, Tribol. Lett. 45 (2012) 357
- [12] D. Mandelli, A. Vanossi, M. Invernizzi, S.V. Paronuzzi Ticco, N. Manini, E. Tosatti, *Superlubric-Pinned Transition in Sliding Incommensurate Colloidal Monolayers*, Phys. Rev. B 92 (2015) 134306
- [13] J. Norell, A. Fasolino, A.S. de Wijn, *Emergent friction in two-dimensional Frenkel-Kontorova models* Phys. Rev. E 94 (2016) 023001
- [14] S.R. Brown, C.H. Scholz, J.B. Rundle, *A simplified spring-block model of earthquakes*, Geophys. Res. Lett. 18 (1991) 215
- [15] Z. Olami, H.J. Feder, K. Christensen, *Self-organized criticality in a continuous, nonconservative cellular automaton modeling earthquakes* Phys. Rev. Lett. 68 (1992) 024301
- [16] V.J. Andersen, *Dynamical mean-field theory for a spring-block model of fracture*, Phys. Rev. B 49 (1994) 9981
- [17] T. Mori, H. Kawamura, *Simulation study of the two-dimensional Burridge-Knopoff model of earthquakes*, J. Geophys. Res. 113 (2008) B06301
- [18] T. Mori, H. Kawamura, *Simulation study of earthquakes based on the two-dimensional Burridge-Knopoff model with long-range interactions*, Phys. Rev. E 77 (2008) 051123
- [19] F. Giacco, M. Pica Ciamarra, L. Saggese, L. de Arcangelis, E. Lippiello, *Non-monotonic dependence of the friction coefficient on heterogeneous stiffness*, Sci. Rep. 4 (2014) 6772
- [20] M.J. Baum, L. Heepe, E. Fadeeva, S.N. Gorb, *Dry friction of microstructured polymer surfaces inspired by snake skin*, Beilstein J. Nanotechnol. 5 (2014) 1091
- [21] B. Yurdumakan, N.R. Raravikar, P.M. Ajayan, A. Dhinojwala, *Synthetic gecko foot-hairs from multiwalled carbon nanotubes*, Chem. Commun. 30 (2005) 3799
- [22] B. Murarash, Y. Itovicha, M. Varenberg, *Tuning elastomer friction by hexagonal surface patterning*, Soft Matters 7 (2011) 5553
- [23] N. Li, E. Xu, Z. Liu, X. Wang, L. Liu, *Tuning apparent friction coefficient by controlled patterning bulk metallic glasses surfaces*, Sci. Rep. 6 (2016) 39388
- [24] K. Autumn, Y. Liang, T. Hsieh, W. Zesch, W.-P. Chan, T. Kenny, R. Fearing, R.J. Full, *Adhesive force of a single gecko foot-hair*, Nature 405 (2000) 681
- [25] M. Varenberg, N. M. Pugno, S.N. Gorb, *Spatulate structures in biological fibrillar adhesion*, Soft Matter 6 (2010) 3269
- [26] P. Stempfle, M. Brendle *Tribological behaviour of nacre-influence of the environment on the elementary wear processes*, Tribol. Int. 39 (2006) 1485
- [27] P. Stempfle, T. Djilali, R. K. Njiwa, M. Rousseau, E. Lopez, X. Bourrat, *Thermal-induced wear mechanisms of sheet nacre in dry friction*, Tribol. Lett. 35 (2009) 97

- [28] D. Labonte, J.A. Williams, W. Federle, *Surface contact and design of fibrillar 'friction pads' in stick insects (Carausius morosus): mechanisms for large friction coefficients and negligible adhesion* J. R. Soc. Interface 11 (2014) 0034
- [29] J.M. Carlson, J.S. Langer, *Properties of earthquakes generated by fault dynamics*, Phys. Rev. Lett. 62 (1989) 2632
- [30] J.M. Carlson, J.S. Langer, B.E. Shaw, *Dynamics of earthquake faults*, Rev. Mod. Phys. 66 (1994) 657
- [31] J. Xia, H. Gould, W. Klein, J.B. Rundle, *Simulation of the Burridge-Knopoff Model of Earthquakes with Variable Range Stress Transfer*, Phys. Rev. Lett. 95 (2005) 248501
- [32] O.M. Braun, I. Barel, M. Urbakh, *Dynamics of Transition from Static to Kinetic Friction*, Phys. Rev. Lett. 103 (2009) 194301
- [33] R. Capozza and M. Urbakh, *Static friction and the dynamics of interfacial rupture*, Phys. Rev. B 86 (2012) 085430
- [34] R. Capozza, S.M. Rubinstein, I. Barel, M. Urbakh, J. Fineberg, *Stabilizing stick-slip friction*, Phys. Rev. Lett. 107 (2011) 024301
- [35] N.M. Pugno, Q. Yin, X. Shi, R. Capozza, *A generalization of the Coulomb's friction law: from graphene to macroscale*, Meccanica 48 (2013) 8
- [36] J. Scheibert, D.K. Dysthe, *Role of friction-induced torque in stick-slip motion*, EPL 92 (2010) 5
- [37] D. S. Amundsen, J. Trømborg, K. Thøgersen, E. Katzav, A. Malthé-Sørenssen, J. Scheibert, *Steady-state propagation speed of rupture fronts along one-dimensional frictional interfaces*, Phys. Rev. E 92 (2015) 032406
- [38] J. Trømborg, H.A. Sveinsson, K. Thøgersen, J. Scheibert, A. Malthé-Sørenssen, *Speed of fast and slow rupture fronts along frictional interfaces* Phys. Rev. E 92 (2015) 012408
- [39] R. Capozza, N.M. Pugno, *Effect of Surface Grooves on the Static Friction of an Elastic Slider*, Tribol. Lett. 58 (2015) 35
- [40] G. Costagliola, F. Bosia, N.M. Pugno, *Static and dynamic friction of hierarchical surfaces*, Phys. Rev. E 94 (2016) 063003
- [41] G. Costagliola, F. Bosia, N.M. Pugno, *Tuning friction with composite hierarchical surfaces*, Tribol. Int. 115 (2017) 261
- [42] G. Costagliola, F. Bosia, N.M. Pugno, *Hierarchical spring-block model for multiscale friction problems*, ACS Biomater. Sci. Eng. 3 (2017) 11
- [43] E. Absi, W. Prager, *Comparison of equivalence and finite element methods*, Comp. Methods. in Appl. Mech. Eng. 6 (1975) 59
- [44] J.R. Rice, A.L. Ruina, *Stability of steady frictional slipping*, J. Appl. Mech. 50 (1983) 343
- [45] J.R. Rice, *Spatiotemporal complexity of slip on a fault*, J. Geophys. Res. 98 (1993) 9885
- [46] A.E. Elbanna, *Pulselike ruptures on strong velocity-weakening frictional interfaces: dynamics and implications* (2011) Doctoral dissertation, California Institute of Technology
- [47] S. Hulikal, K. Bhattacharya, N. Lapusta, *Collective behavior of viscoelastic asperities as a model for static and kinetic friction*, J. Mech. Phys. Solids 76 (2015) 144
- [48] J.H. Dieterich, *Modeling of rock friction: 1. Experimental results and constitutive equations*, J. Geophys. Res. 84 (1979) 2161
- [49] J.R. Rice, N. Lapusta, K. Ranjith, *Rate and state dependent friction and the stability of sliding between elastically deformable solids*, J. Mech. Phys. Solids 49 (2001) 1865
- [50] T.H. Heaton, *Evidence for and implications of self-healing pulses of slip in earthquake rupture*, Phys. Earth Planet In. 64 (1990) 1
- [51] G. Zheng, J.R. Rice, *Conditions under which velocity-weakening friction allows a self-healing versus a cracklike mode of rupture*, Bull. Seismol. Soc. Am. 88 (1998) 1466
- [52] A.E. Elbanna, T.H. Heaton, *A new paradigm for simulating pulse-like ruptures: the pulse energy equation*, Geophys. J. Int. 189 (2012) 1797
- [53] S.C. Hunter, *The rolling contact of a rigid cylinder with a viscoelastic half space*, J. Appl. Mech. 28 (1961) 611
- [54] N. W. Tschoegl, *The Phenomenological Theory of Linear Viscoelastic Behavior*, Springer Verlag (1989)
- [55] B.N.J. Persson, *Theory of rubber friction and contact mechanics*, J. Chem. Phys. 115 (2001), pp. 3840
- [56] H.T. Banks, S. Hu, Z.R. Kenz, *A Brief Review of Elasticity and Viscoelasticity for Solids*, Adv. Appl. Math. Mech 3 (2011) 1
- [57] A.O. Krushynska, V.G. Kouznetsova, M.G.D. Geers, *Visco-elastic effects on wave dispersion in three-phase acoustic metamaterials* J. Mech. and Phys. of Solids 96 (2016) 29

- [58] G. Carbone, C. Putignano, *A novel methodology to predict sliding and rolling friction of viscoelastic materials: Theory and experiments*, J. Mech. and Phys. of Solids 61 (2013) 1822
- [59] S.M. Rubinstein, G. Cohen, J. Fineberg, *Dynamics of Precursors to Frictional Sliding*, Phys. Rev. Lett. 98 (2007) 226103
- [60] O. Ben-David, G. Cohen, J. Fineberg, *The Dynamics of the Onset of Frictional Slip* Science 330 (2010) 211
- [61] I. Svetlizky, J. Fineberg, *Classical shear cracks drive the onset of dry frictional motion*, Nature 509 (2014) 205
- [62] I. Svetlizky, D. Pino Munoz, M. Radiguet, D. S. Kammer, J. F. Molinari, J. Fineberg, *Properties of the shear stress peak radiated ahead of rapidly accelerating rupture fronts that mediate frictional slip*, PNAS 113 (2016) 542-547
- [63] E. Bayart, I. Svetlizky, J. Fineberg, *Fracture mechanics determine the lengths of interface ruptures that mediate frictional motion* Nature Physics 12 (2016) 166
- [64] D.S. Kammer, M. Radiguet, J.P. Ampuero, J.F. Molinari, *Linear elastic fracture mechanics predicts the propagation distance of frictional slip*, Tribol. Lett. 57 (2015) 23
- [65] M. Radiguet, D.S. Kammer, P. Gillet, J.F. Molinari, *Survival of heterogeneous stress distributions created by precursory slip at frictional interfaces*, Phys. Rev. Lett. 111 (2013) 164302
- [66] N. Lapusta, J.R. Rice, *Nucleation and early seismic propagation of small and large events in a crustal earthquake model* J. Geophys. Res. 108 (2003) 2205
- [67] M. Urbakh, J. Klafter, D. Gourdon, J. Israelachvili *The nonlinear nature of friction*, Nature 430 (2004)
- [68] B. He, W. Chen, Q.J. Wang, *Surface Texture Effect on Friction of a Microtextured Poly(dimethylsiloxane) (PDMS)*, Trib. Lett. 31 (2008) 187
- [69] N.B. Tay, M. Minn, S.K. Sinha, *A Tribological Study of SU-8 Micro-Dot Patterns Printed on Si Surface in a Flat-on-Flat Reciprocating Sliding Test* Trib. Lett. 44 (2011) 167
- [70] C. Greiner, M. Schafer, U. Pop, P. Gumbsch, *Contact splitting and the effect of dimple depth on static friction of textured surfaces*, Appl. Mater. Interfaces 6 (2014) 7986